BioMedical Engineering OnLine

RESEARCH

Open Access

Early diagnostic model of pyonephrosis with calculi based on radiomic features combined with clinical variables

Yongchao Yan[1†], Yunbo Liu[1†], Yize Guo[1], Bin Li[1], Yanjiang Li[1*] and Xinning Wang[1*]

[†]Yongchao Yan and Yunbo Liu have contributed equally to this work.

*Correspondence: lyj2001353@163.com; wxn1992@126.com

[1] The Affiliated Hospital of Qingdao University, Qingdao, Shandong, China

Abstract

Objective: This retrospective aims to develop a comprehensive predictive model based on CT radiomic features and clinical parameters, facilitating early preoperative diagnosis of pyonephrosis.

Methods: Clinical and radiological data from 311 patients treated for upper urinary tract stones with obstructive pyelohydronephrosis, between January 2018 and May 2023, were retrospectively collected. Univariate and multivariate logistic regression analyses were conducted on clinical data to identify independent risk factors for pyonephrosis. A clinical model was developed using logistic regression. The 3D Slicer software was employed to manually delineate the region of interest (ROI) in the preoperative CT images, corresponding to the area of pyelohydronephrosis, for feature extraction. The optimal radiomic features were selected to construct radiomic models and calculate the radiomic score (Radscore). Subsequently, a combined clinical–radiomic model—the nomogram—was established by integrating the Radscore with independent risk factors.

Results: Univariate and multivariate logistic regression analyses identified cystatin C, Hounsfield Unit (HU) of pyonephrosis, history of ipsilateral urological surgery, and positive urine culture as independent risk factors for pyonephrosis ($P < 0.05$). Fourteen optimal radiomic features were selected from CT images to construct four radiomic models, with the Naive Bayes model demonstrating the best predictive performance in both training and validation sets. In the training set, the AUCs for the clinical model, radiomic model, and nomogram were 0.902, 0.939, and 0.991, respectively; in the validation set, they were 0.843, 0.874, and 0.959. Both calibration and decision curves showed good agreement between the predicted probabilities of the nomogram and the actual occurrences.

Conclusion: The nomogram, constructed from CT radiomic features and clinical variables, provides an effective non-invasive predictive tool for pyonephrosis, surpassing both clinical and radiomic models.

Keywords: Pyonephrosis, Upper urinary tract calculi, Radiomics, Machine learning, Preoperative diagnosis

Introduce

Urinary tract lithiasis ranks among the most prevalent diseases of the urinary system, with upper urinary tract stones being the most common [1]. Studies indicate that 3.2% of patients with upper urinary tract stones develop obstructive pyonephrosis [2].

Pyonephrosis refers to the accumulation of purulent exudate within the renal pelvis and collecting system. Renal abscess can cause the following changes: 1. renal tissue destruction: infection and inflammation can lead to the destruction of renal parenchyma, possibly resulting in renal tissue necrosis. The renal tubules and nephrons may be damaged, affecting renal function. 2. Pelvic dilation: due to the accumulation of pus, the renal pelvis can significantly dilate. This dilation can compress the renal parenchyma, further impairing renal function. 3. Fibrosis and scar formation: with ongoing infection, fibrosis and scar tissue may develop in the kidney. These changes can lead to permanent structural alterations and functional impairment of the kidney. Renal tissue destruction: infection and inflammation can lead to the destruction of renal parenchyma, possibly resulting in renal tissue necrosis. The renal tubules and nephrons may be damaged, affecting renal function [3]. Pyonephrosis is a severe condition often associated with pyelonephritis, where the kidney becomes distended with pus. The clinical manifestation typically includes flank pain, fever, and other systemic symptoms. In a recent descriptive study, Praveen Kumar et al. (2023) found that flank pain with or without fever was the most common symptom among patients with pyonephrosis in the context of pyelonephritis [4].

Obstructive pyonephrosis due to stones is a severe urological condition that presents heterogeneously; minor cases may only manifest asymptomatic bacteriuria while severe ones can rapidly progress to sepsis, leading to loss of renal function in a short period [5]. Without timely intervention, the condition may deteriorate into urosepsis, posing a severe threat to patient survival and imposing significant burdens on society and families [6, 7]. However, because of the widespread use of broad-spectrum antimicrobials, some patients with pyonephrosis may not exhibit any conspicuous symptoms or signs, complicating the early identification of affected individuals [8]. Some patients receive a definitive diagnosis of pyonephrosis during surgery, and inadequate perioperative preparation increases their risk of postoperative systemic inflammatory response syndrome (SIRS) [9]. Pyonephrosis is a medical condition that requires urgent treatment, typically necessitating antibiotic therapy and potential surgical intervention (such as drainage of pus or relief of urinary obstruction). Early diagnosis and treatment are crucial to prevent further deterioration of kidney function and the occurrence of systemic complications (such as sepsis).

With the continual advancement of computer technology, radiomics has been widely applied in the diagnosis, differential diagnosis, and prognosis assessment of diseases. Wang et al. [10] constructed a radiomics–clinical model using CT radiomics and clinical variables that demonstrated good accuracy in predicting uric acid stones. Xu L et al. [11] developed a predictive model for the WHO/ISUP grading of clear cell renal cell carcinoma based on CT radiomics, exhibiting commendable diagnostic efficacy.

Although articles predicting pyonephrosis using imaging features already exist [12], on one hand, the predictive values of these articles are not very high, and on the other hand, patients with pyonephrosis inevitably have a certain systemic response due to the

accumulation of a large amount of infectious pus. Therefore, we believe that combining systemic blood indicators with imaging indicators to predict pyonephrosis may provide better predictive value. This study aims to construct a comprehensive model by integrating radiomics features with clinical variables to assist clinicians in the early non-invasive diagnosis of stonogenic pyonephrosis. This model is intended to facilitate early clinical intervention for stonogenic pyonephrosis, enabling the formulation of personalized treatment plans to prevent severe complications such as urosepsis and improve patient outcomes.

Materials

Study subjects

This study retrospectively collated and analyzed clinical data and non-contrast CT imaging records of 311 patients with upper urinary tract stones complicated by pelvicalyceal distention treated at our center from January 2018 to May 2023. Among these, 95 patients were identified with pyonephrosis, while 216 did not have the complication. The study was conducted in accordance with the principles of the Declaration of Helsinki and was approved by the ethics committee of our center. All patients underwent retrograde ureteral stenting (RUS), ureteroscopic lithotripsy (URSL), percutaneous nephrostomy (PCN), or percutaneous nephrolithotomy (PCNL).

Inclusion criteria

(1) Patients aged $\geq$ 18 years;
(2) Patients with upper urinary tract stones;
(3) Patients with complete baseline clinical data;
(4) Patients who underwent surgical drainage or procedures (RUS, URSL, PCN, or PCNL) at our center.

Exclusion criteria

(1) Absence of significant hydronephrosis in the affected kidney;
(2) History of endoscopic surgery prior to admission, treated for residual stones upon admission;
(3) Incomplete baseline clinical data in medical records;
(4) Prior nephrostomy or retrograde ureteral stent placement before admission;
(5) Congenital urological anomalies (such as horseshoe kidney, ectopic kidney, polycystic kidney, duplicated kidney, or solitary kidney);
(6) Concomitant other urological diseases (infections, tuberculosis, tumors, etc.);
(7) Poor quality CT images affecting the delineation of the region of interest (ROI).

(For the specific inclusion and exclusion criteria, please refer to Fig. 1.)

Diagnostic criteria for study subjects

The diagnosis of study subjects must fulfill the following two criteria: 1. presence of upper urinary tract calculi. All patients included in the study were confirmed to have varying

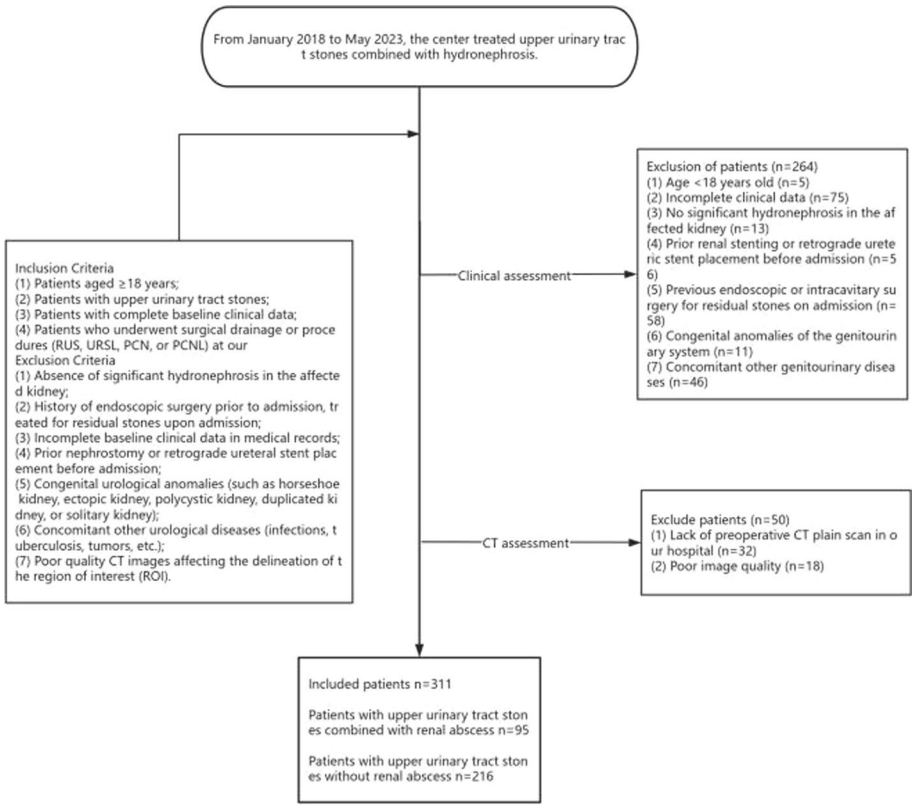

Fig. 1 The specific inclusion and exclusion criteria

degrees of renal and ureteral calculi via radiological examinations such as urological ultrasound, non-contrast computed tomography (CT), etc. Other potential diseases, such as urinary system tumors, were excluded. 2. Presence of renal abscess. Purulent, viscous pus/purulent collections were observed grossly during retrograde ureteral stent placement or percutaneous nephrostomy, usually with positive pus cultures.

Clinical data of study subjects

Patient clinical data were collected through our center's data management platform, including: age, gender, laterality, body mass index (BMI), renal colic, fever, history of ipsilateral urologic surgery, diabetes, hypertension, staghorn calculi, degree of pelvicalyceal dilatation, severe hydronephrosis or atrophy of the contralateral kidney (SHACK), Hounsfield Unit (HU) of pelvicalyceal effusion, stone density, maximum stone size, preoperative serum uric acid, blood urea nitrogen, blood urea nitrogen/creatinine, serum creatinine, cystatin C, preoperative white blood cells, monocytes, neutrophils, lymphocytes, platelets, neutrophil–lymphocyte ratio (NLR), lymphocyte–monocyte ratio (LMR), platelet–lymphocyte ratio (PLR), urinary white blood cells, urinary nitrites, and urine culture.

Results

Clinical variables of patients

This study incorporated a total of 311 subjects, who were categorized into two groups based on the presence of renal abscess: the renal abscess group ($n=95$) and the

non-renal abscess group ($n=216$). Statistical analysis was conducted on the preoperative baseline characteristics of the patients, revealing that there were no significant differences between the two groups in terms of age, BMI, side of stone, hypertension, staghorn calculi, hydronephrosis, SHACK, stone density, and maximum stone diameter ($P>0.05$). However, significant differences were observed between the groups in gender, renal colic, fever, history of ipsilateral urological surgery, diabetes, and CT attenuation of hydronephrosis ($P<0.05$), as detailed in Table 1.

Comparisons of laboratory test results between the two groups are shown in Table 2. Statistically significant differences were found in urea nitrogen, serum creatinine, albumin, cystatin C, white blood cells, neutrophils, lymphocytes, monocytes, NLR, LMR, PLR, urinary white blood cells, urinary nitrites, and urine culture ($P<0.05$). There was no statistical difference between the groups regarding the urea nitrogen/creatinine ratio, serum uric acid, and platelets ($P>0.05$).

Training set single-factor and multi-factor logistic regression analysis shows that the CT value of renal pelvis fluid (OR: 1.033; 95% CI 1.026–1.039; $P<0.001$), history of same-side urological surgery (OR: 1.095; 95% CI 0.892–1.074; $P=0.043$), cystatin C (OR: 1.115; 95% CI 1.029–1.208; $P=0.026$), urine culture (OR: 1.218; 95% CI 1.121–1.324; $P<0.001$) are independent risk factors for patients with perirenal abscess caused by stones, as shown in Table 3.

Feature selection and construction of radiomics model

A total of 1834 radiomics features were extracted from each patient's CT images using Gaussian-Laplace filters and wavelet filters. ANOVA and LASSO (Fig. 2A and B) with tenfold cross-validation retained 14 features (Fig. 3). Four machine learning models were tested in the training and validation sets, with corresponding results presented in Tables 2S and 3S. The Naive Bayes (NB) model demonstrated the best performance on the validation set and showed similar, stable results on both the training and validation sets (Fig. 1S). Consequently, the NB model was used to establish a predictive model for the selected feature parameters and to calculate a radiomics score (Radscore) for each sample, reflecting the risk of nephrolithiasis-associated renal abscess. The Radscore is the sum of the radiomics features and corresponding coefficients used to construct the model, formulated as $\text{Radscore} = \text{intercept} + \Sigma\beta i \times Xi$. The coefficients for each feature are listed in Table 4S.

Development and evaluation of the comprehensive model

The final comprehensive model (nomogram model) included the CT attenuation of hydronephrosis, history of ipsilateral urological surgery, cystatin C, urine culture, and Radscore, as shown in Fig. 4A. Figure 4B and C depicts the calibration curves for the clinical model, radiomics model, and nomogram model. The calibration curve and Hosmer–Lemeshow test of the nomogram model indicated good calibration and fit, outperforming the other models. Figure 5A and B details the nomogram model scores for each patient in the training and test sets. Tables 5S and 4 provide a comprehensive summary of the diagnostic performance of the clinical model, radiomics model, and nomogram model in both sets. The ROC curves of the models are illustrated in Fig. 6A and B. DeLong's test revealed that the nomogram model's diagnostic capability

Table 1 Basic characteristics of renal abscess group and non-renal abscess group

Variable	Non-renal abscess group($n=216$)	Renal abscess group($n=95$)	*P-value*
Age (years)	54.00 ± 11.74	58.77 ± 12.12	0.421
BMI(kg/ m2)	25.05 ± 3.70	25.14 ± 3.60	0.51
Gender (n, %)			0.01
Female	74(34.26)	48(50.53)	
Male	142(65.74)	47(49.47)	
Sides (n,%)			0.228
Left	112(51.85)	57(60.00)	
Right	104(48.15)	38(40.00)	
Renal colic (n,%)			0.002
No	146(67.59)	46(48.42)	
Yes	70(32.41)	49(51.58)	
Fever (n, %)			< 0.001
No	210(97.22)	67(70.53)	
Yes	6(2.78)	28(29.47)	
History of same-side urological surgery (n, %)			0.007
No	164(75.93)	57(60.00)	
Yes	52(24.07)	38(40.00)	
Diabetes (n, %)			0.001
No	187(86.57)	67(70.53)	
Yes	29(13.43)	28(29.47)	
Hypertension (%)			0.105
No	164(75.93)	63(66.32)	
Yes	52(24.07)	32(33.68)	
Staghorn stone (%)			0.547
No	189(87.50)	80(84.21)	
Yes	27(12.50)	15(15.79)	
Hydronephrosis (n, %)			0.136
Mild/moderate	137(63.43)	51(53.68)	
Severe	79(36.57)	44(46.32)	
Shock (n,%)			0.27
No	208(96.30)	88(92.63)	
Yes	8(3.70)	7(7.37)	
Renal pelvis fluid CT value (HU)	6.16 ± 4.52	14.17 ± 5.39	< 0.001
Density of stones (HU)	942.83 ± 91.81	854.34 ± 85.72	0.935
Maximum stone diameter (mm)	16.21 ± 9.42	16.28 ± 9.98	0.95

was significantly superior to both the clinical and radiomics models in the training set ($P<0.001$, $P=0.006$), while the difference between the diagnostic capabilities of the radiomics and clinical models was not statistically significant ($P=0.283$). In the validation set, the clinical model's diagnostic performance was slightly inferior to the radiomics model, but the difference was not significant ($P=0.646$). Both the radiomics model and the clinical model were inferior to the nomogram model, with the difference being statistically significant ($P=0.001$, $P=0.047$).

In summary, the nomogram model demonstrated the highest diagnostic efficiency in both the training and validation sets. Additionally, Fig. 3C and D further illustrates the decision curve analysis (DCA) of the three models, indicating that the overall net benefit

Table 2 Comparison of laboratory test results between renal abscess group and non-renal abscess group

Variable	Non-renal abscess group(n = 216)	Renal abscess group(n = 95)	*P-value*
Urea nitrogen (mg/dl)	6.06 (4.96,6.98)	6.55 (5.50,9.52)	< 0.001
Urea nitrogen / creatinine	16.92 (13.71,21.56)	15.74 (13.16,21.67)	0.356
Blood creatinine (μ mol/L)	87.35 (70.00,100.40)	101.65 (81.65,135.95)	< 0.001
Blood uric acid (μ mol/L)	362.47 (301.60,419.95)	359.12 (289.68,400.15)	0.77
Albumin (g/L)	42.75 (39.99,45.74)	37.96 (32.60,41.93)	< 0.001
Cystatin C (mg/L)	0.96 (0.83,1.06)	1.34 (1.08,1.41)	< 0.001
WBC(× 10^9/L)	6.91 (5.65,8.03)	9.12 (6.51,12.19)	< 0.001
Neutrophils(× 10^9/L)	4.02 (3.28,5.10)	6.68 (4.32,10.31)	< 0.001
Lymphocytes(× 10^9/L)	1.92 (1.62,2.39)	1.42 (0.87,2.04)	< 0.001
Mononuclear cells(× 10^9/L)	0.47 (0.39,0.58)	0.58 (0.41,0.82)	< 0.001
Platelets (× 10^9/L)	236.00 (195.50,281.25)	245 (181.25,298.25)	0.873
NLR	2.05 (1.48,2.54)	3.98 (2.52,10.63)	< 0.001
PLR	122.21 (97.76,153.67)	168.43 (124.84,243.90)	< 0.001
LMR	4.25 (3.12,5.48)	2.71 (1.36,4.03)	< 0.001
White blood cells in urine (n,%)			< 0.001
Negative	102 (47.22)	18 (18.95)	
Positive	114 (52.78)	77 (81.05)	
Urinary nitrite (n,%)			< 0.001
Negative	199 (92.13)	68 (71.58)	
Positive	17 (7.87)	27 (28.42)	
Urine culture (n,%)			< 0.001
Negative	180 (83.33)	35 (36.84)	
Positive	36 (16.67)	60 (63.16)	

of the radiomics and nomogram models in distinguishing nephrolithiasis-associated renal abscesses was significantly higher than that of the clinical model. This finding has important clinical value for enhancing the diagnostic accuracy of renal abscesses.

Discussion

Hydronephrosis is the dilation of the renal pelvis and calyces secondary to upper urinary tract obstruction, commonly following urolithiasis [1]. Renal abscess refers to the purulent parenchymal lesion developing on the basis of hydronephrosis [13]. The clinical manifestations of nephrolithiasis-related renal abscess can vary from asymptomatic bacteriuria to severe pyonephrosis, with nonspecific complaints and clinical symptoms possibly being the sole indicators in some patients [14]. The application of broad-spectrum antibiotics has led to atypical clinical presentations in as many as 15% of patients, posing new challenges in the diagnosis of nephrolithiasis-associated renal abscess. Renal abscess is a urological emergency that can lead to renal parenchymal destruction, loss of renal function, rapid progression to urosepsis, and even septic shock. Early diagnosis and treatment are critical for preserving renal function and improving prognosis. However, the current clinical diagnosis of nephrolithiasis-associated renal abscess still relies on the comprehensive analysis and judgment by experienced clinicians based on the patient's clinical data, laboratory tests, and imaging findings. Hence, this study

Table 3 Logistic analysis results of clinical variables in the training set

Variable	Univariate analysis		Multivariable analysis	
	OR(95% CI)	*P-value*	OR(95% CI)	*P-value*
Age	1.004 (1.000–1.008)	0.081		
BMI	1.007 (0.993–1.021)	0.399		
Gender	0.782 (0.708–0.865)	< 0.001	0.978 (0.892–1.074)	0.696
Sides	1.008 (0.910–1.116)	0.898		
Renal colic	1.199 (1.080–1.331)	0.005	1.039 (0.968–1.116)	0.374
Fever	1.743 (1.496–2.032)	< 0.001	1.09 (0.959–1.239)	0.267
History of same-side urological surgery	1.244 (1.114–1.390)	< 0.001	1.095 (1.018–1.177)	0.043
Diabetes	1.251 (1.104–1.418)	0.003	1.042 (0.96–1.133)	0.408
Hypertension	1.092 (0.971–1.228)	0.216		
Staghorn stone	1.059 (0.923–1.214)	0.491		
Hydronephrosis	1.076 (0.970–1.194)	0.240		
SHACK	1.149 (0.919–1.435)	0.304		
Renal pelvis fluid CT value (HU)	1.049 (1.043–1.057)	< 0.001	1.033 (1.026–1.039)	< 0.001
Density of stones (HU)	1.000 (0.999–1.001)	0.883		
Maximum stone diameter (mm)	1.000 (0.994–1.005)	0.896		
Urea nitrogen (mg/dl)	1.020 (1.011–1.029)	< 0.001	0.989 (0.975–1.003)	0.202
Urea nitrogen / creatinine	0.998 (0.991–1.005)	0.618		
Blood creatinine (μ mol/L)	1.001 (1.000–1.001)	< 0.001	1.0 (1.0–1.001)	0.521
Blood uric acid (μ mol/L)	1.000 (0.999–1.000)	0.601		
Albumin (g/L)	0.964 (0.957–0.972)	< 0.001	0.998 (0.99–1.005)	0.599
Cystatin C (mg/L)	1.383 (1.262–1.514)	< 0.001	1.115 (1.029–1.208)	0.026
WBC(× 10^9/L)	1.60 (1.36–1.87)	< 0.001	1.10 (0.27–4.55)	0.898
Neutrophils(× 10^9/L)	1.76 (1.46–2.13)	< 0.001	1.01 (0.99–1.02)	0.487
Lymphocytes(× 10^9/L)	0.833 (0.780–0.889)	< 0.001	0.79 (0.638–0.978)	0.071
Mononuclear cells(× 10^9/L)	1.627 (1.306–2.028)	< 0.001	0.913 (0.67–1.245)	0.628
Platelets (× 10^9/L)	1.000 (1.000–1.001)	0.593		
NLR	1.021 (1.016–1.026)	< 0.001	0.997 (0.989–1.004)	0.452
PLR	1.002 (1.001–1.002)	< 0.001	1.0 (1.0–1.001)	0.137
LMR	0.929 (0.907–0.952)	< 0.001	1.021 (0.982–1.062)	0.378
White blood cells in urine	1.316 (1.189–1.455)	< 0.001	1.071 (0.995–1.151)	0.125
Urinary nitrite	1.411 (1.226–1.623)	< 0.001	1.036 (0.933–1.149)	0.576
urine culture	1.585 (1.438–1.747)	< 0.001	1.218 (1.121–1.324)	< 0.001

developed a classification model based on clinical variables and CT radiomics features to achieve precise preoperative prediction of nephrolithiasis-related renal abscess, thereby enhancing diagnostic accuracy and reliability.

In this study, a statistical analysis of clinical variables from two patient cohorts revealed that ipsilateral urological surgery history, cystatin C levels, renal pelvis hydronephrosis CT values, and positive urine cultures stand as independent risk factors for nephropyonephrosis, aligning with findings from most research. Patodia et al. [15] discovered a correlation between ipsilateral urological surgery history and pyonephrosis after analyzing data from 401 non-pyonephrotic and 91 pyonephrotic urological patients. This may be attributed to urinary tract damage caused by urological procedures and instruments, leading to alterations in anatomical structures and urinary system dysfunction. These changes could obstruct normal urine flow, elevating the risk of urinary infections and

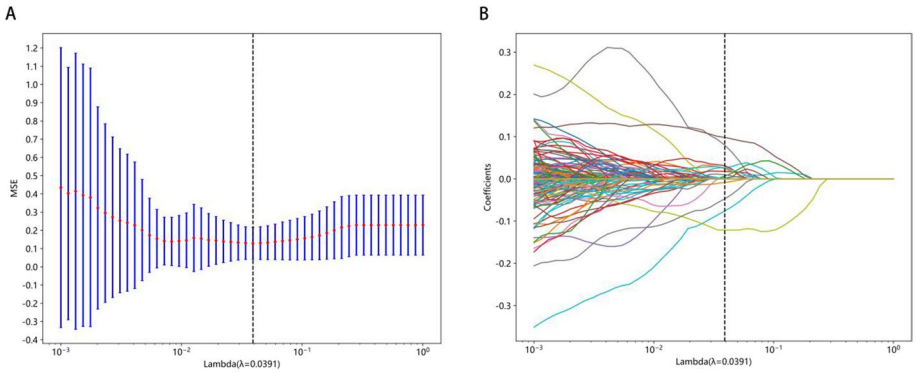

Fig. 2 Feature selection of imaging genomics based on LASSO regression model. **A**: Selection of tuning parameter (λ). Use Lasso regression model and perform tenfold cross-validation based on the minimum standard. The optimal value of λ is represented by a vertical dashed line, $\lambda = 0.0391$. **B**: Lasso coefficient distribution for 1834 radiomic features. Vertical dashed line is drawn using the 14 selected radiomic features

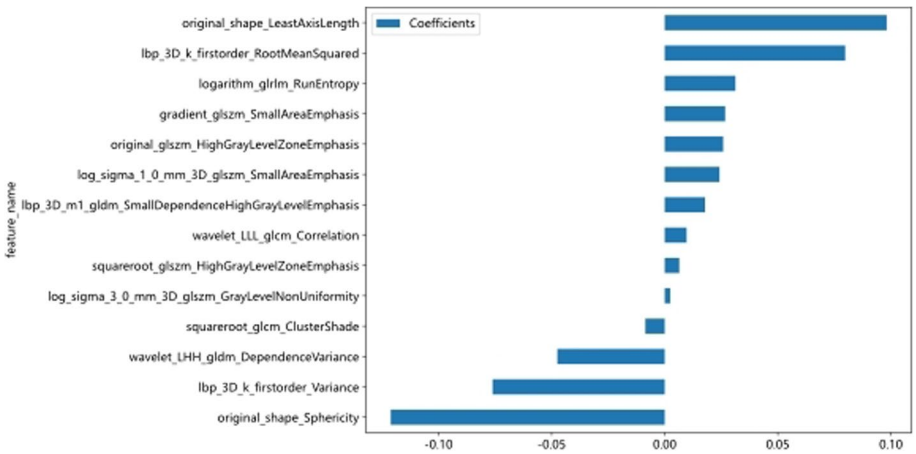

Fig. 3 The 14 selected radiomic features and their corresponding coefficients

Table 4 Comparison of predictive capabilities of three models in the validation set

Model	Validation set(n = 94)					
	AUC (95%CI)	Sensitivity	Specificity	Accuracy	PPV	NPV
Clinical model	0.843 (0.752–0.933)	0.818	0.820	0.819	0.711	0.893
Imaging omics model	0.874 (0.786–0.961)	0.818	0.803	0.809	0.692	0.891
Line chart model	0.959 (0.922–0.995)	0.848	0.918	0.894	0.848	0.918

stone obstructions, potentially culminating in pyonephrosis. Cystatin C, a low-molecular-weight protein metabolized primarily by the kidneys and almost entirely cleared by glomerular filtration, is reabsorbed and broken down in the proximal renal tubules without re-entry into the bloodstream [16]. Under physiological conditions, cystatin C levels are less affected by non-GFR factors such as gender, age, hormonal fluctuations, and alcohol intake compared to creatinine [17, 18], making it an ideal biomarker for assessing glomerular filtration rates. Studies indicate that pyonephrosis refers to

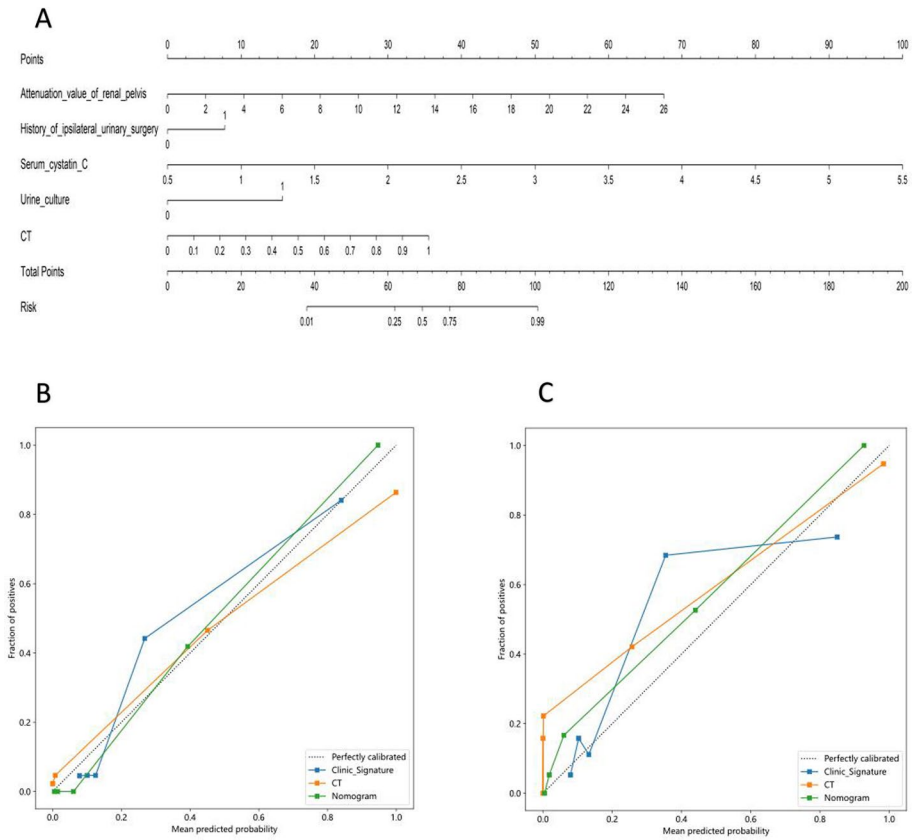

Fig. 4 Line chart model and calibration curves of three models. **A**: Line chart model, **B**: calibration curves of three models on the training set, **C**: calibration curves of three models on the validation set. The 45-degree dashed line represents ideal prediction. The calibration curve of the line chart model shows good consistency between the training set and the validation set, being the best among the three models

infective hydronephrosis with renal parenchymal suppuration and loss of renal function [19], hence, cystatin C levels in the body may rise, possibly due to reduced clearance as a result of glomerular filtration impairment from renal parenchymal damage in nephropyonephrosis. Traditionally, CT scans were used to assess renal pelvis hydronephrosis, relying on nonspecific indicators like thickening of the renal pelvis and ureter walls, renal enlargement, striated changes in renal parenchyma, and perirenal fat deposition, limiting diagnostic efficacy [20]. Yet, recent studies have shown that renal pelvis hydronephrosis CT values can differentiate between hydronephrosis and pyonephrosis. Emrah et al. [21] demonstrated that a CT value of renal pelvis hydronephrosis at or exceeding 9.21 HU accurately diagnoses pyonephrosis, with a sensitivity of 65.96% and a specificity of 87.93%.

In the field of nephropyelitis secondary to kidney stones, there are currently few academic studies on radiomics. Past studies have focused on constructing models based on clinical or radiographic features for predicting nephropyonephrosis. Liu H et al. [22] statistically analyzed clinical data from 322 patients with and without pyonephrosis, building a support vector machine (SVM) model for predicting nephropyonephrosis in upper urinary tract stone patients. Basmaci et al. [23] retrospectively analyzed the renal pelvis hydronephrosis attenuation values of 51 patients to construct a predictive model based

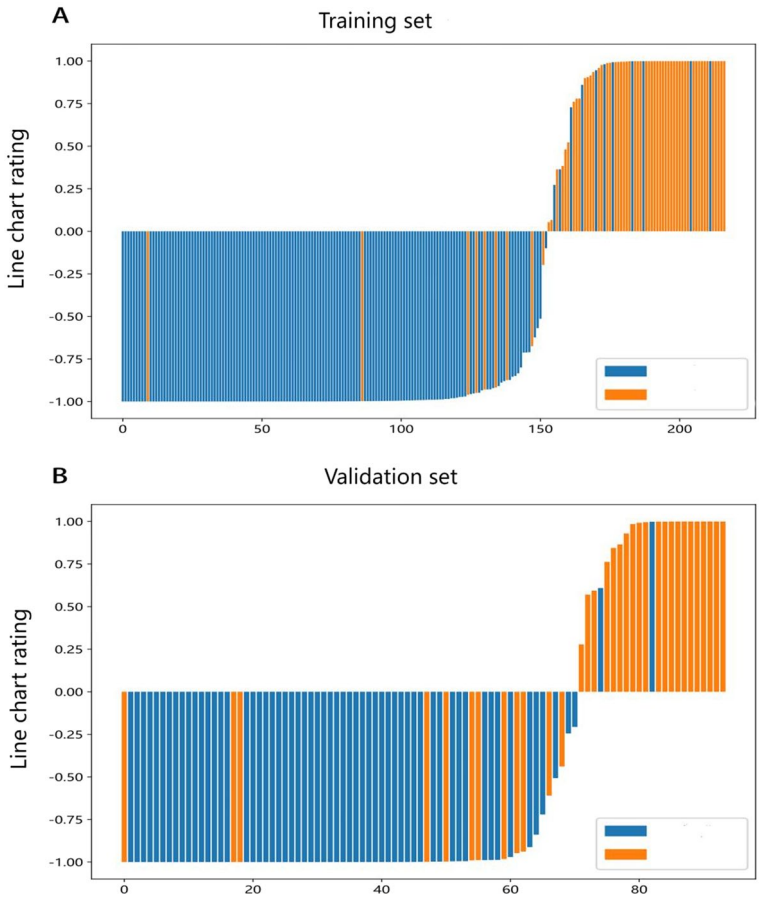

Fig. 5 Column chart scores for each patient. Column chart scores for each patient in the **A** and **B** training and validation sets. The blue bars represent scores for non-renal abscess patients, and the yellow bars represent scores for renal abscess patients

on a single radiographic feature. Wang Xinguang et al. [24] collected clinical features from 322 patients with obstructive hydronephrosis and constructed five machine learning models based on multiple clinical features, achieving better predictive results compared to traditional models.

This study marks the inaugural application of radiomics to the preoperative prediction of nephrolithiasis-associated pyonephrosis, developing four radiomic models based on 14 radiomic features extracted from CT images using machine learning algorithms. Logistic regression (LR) is a statistical-based machine learning algorithm for classification tasks, mapping linear regression outcomes to the [0, 1] interval through a logistic function, thus fulfilling binary classification objectives. Due to its simplicity and clinical ubiquity, LR has witnessed widespread adoption. Support Vector Machine (SVM) is a supervised learning algorithm designed for binary and multi-class tasks, operating on the principle of finding an optimal hyperplane in feature space to accurately classify data [25]. Random Forest (RF), a supervised ensemble algorithm, constructs multiple decision trees and amalgamates their predictions to form a definitive predictive model [26]. RF is adept at managing classification and regression tasks, significantly mitigating the risk of model overfitting due to decision tree data overfitting and thus enhancing model

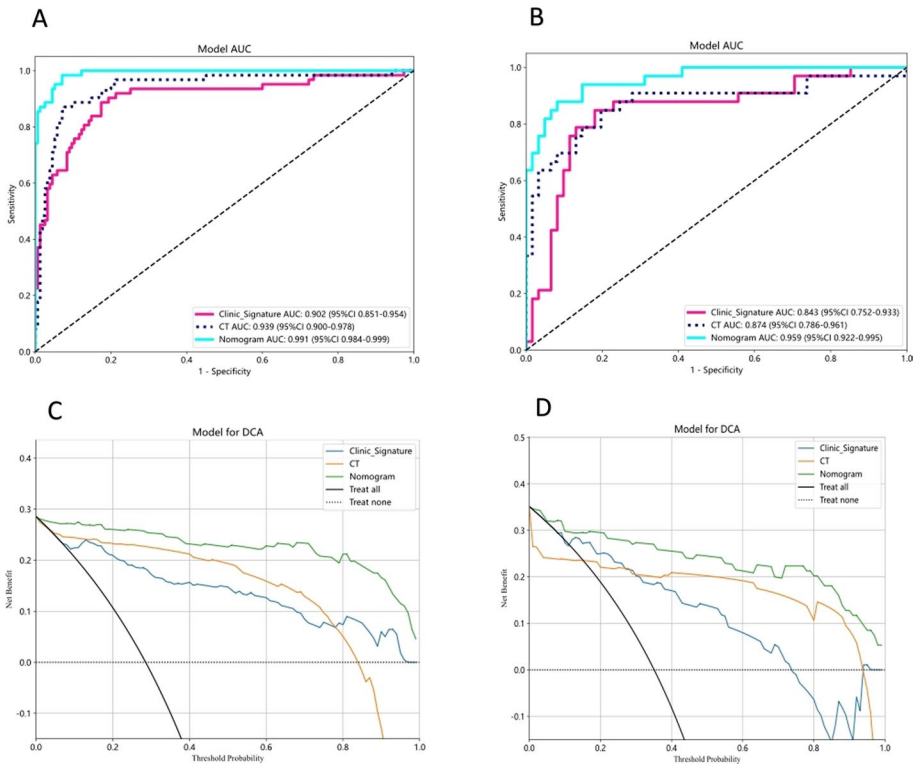

Fig. 6 ROC curve and decision curve analysis of different models in the training set and validation set. **A**: ROC curve of the training set, **B**: ROC curve of the validation set, **C**: decision curve analysis of the training set, **D**: decision curve analysis of the validation set

generalizability [27, 28]. Naive Bayes (NB) is a probability-based classification technique that employs Bayesian theorem and the assumption of feature conditional independence for probabilistic computations and inference, known for its simplicity, intuitive nature, and high computational efficiency, especially in text classification and natural language processing [29]. Kim et al. [30] utilized various machine learning algorithms, including SVM, RF, and NB, to construct a radiomics-based machine learning model distinguishing COVID-19 from pneumonia on chest X-rays. In this study's training set, the AUC values for the LR, SVM, RF, and NB models were 0.942, 0.982, 0.916, and 0.939, respectively; in the validation set, they were 0.762, 0.794, 0.808, and 0.874, respectively. Notably, all models outperformed LR in the validation set, demonstrating the superiority of other machine learning algorithms over traditional regression methods in dealing with complex, high-dimensional data. The NB model exhibited the best predictive efficacy, with AUC values of 0.939 and 0.874 in the training and validation sets, respectively, which led to its selection for constructing a comprehensive model and calculating Radscore.

Incorporating clinical variables and radiomic features, a nomogram model was constructed, and its diagnostic performance was compared with that of three models. In the training set, the AUC values for the clinical, radiomic, and nomogram models were 0.902, 0.939, and 0.991, respectively; in the validation set, they were 0.843, 0.874, and 0.959, respectively. The study found that, in both the training and validation sets, the

nomogram model's diagnostic performance surpassed that of the radiomic and clinical models. Therefore, the study concludes that the nomogram model provides an accurate, objective, non-invasive diagnostic method for the early detection of nephrolithiasis-associated pyonephrosis, offering valuable insights for clinical decision-making and personalized treatment, thereby improving patient prognosis.

Despite the significant advancements over traditional models in predicting nephrolithiasis-associated pyonephrosis, our study has limitations. Firstly, being retrospective, it is prone to selection bias. Secondly, manual segmentation of the lesion ROI is subject to subjective variability. Moreover, as a single-center study with a small sample size, it lacks multi-center validation. Future endeavors could involve collaboration with other centers to enhance the predictive model's applicability.

Conclusion

The nomogram model, constructed from CT radiomic features and clinical risk factors, effectively predicts nephrolithiasis-associated pyonephrosis non-invasively. Compared to standalone clinical or radiomic models, it boasts higher predictive accuracy. The application of the nomogram model provides clinicians with additional references for clinical decisions, allowing for early identification and intervention in patients with nephrolithiasis-associated pyonephrosis, devising personalized treatment plans, improving patient outcomes, and preventing severe complications such as pyosepticemia.

Research methods

Image acquisition and segmentation

The scanning range spanned from the upper pole of the kidney to the lower edge of the ischial tuberosity, with all patients undergoing a 64-layer multi-detector CT scan (GE Medical, Discovery CT 750HD). The CT image acquisition parameters were as follows: tube voltage ranged from 100-120 kV, and automatic tube current varied between 200–350 mA. During scanning, the rotation time was set to 0.5 s, with both scanning slice thickness and reconstruction slice thickness standardized at 5 mm.

Lesions were delineated by at least two experienced physicians using the open-source radiomics software 3D Slicer to trace the region of interest (ROI) layer by layer in the DICOM format of the CT images of patients with pelvicalyceal effusion. Image segmentation was performed independently by two radiologists with extensive experience. They were blinded to the patients' histopathology. One of the radiologists (radiologist A, with 7 years of experience) manually drew the ROI slice by slice using the open-source software 3D Slicer 4.11.0 (https://www.slicer.org/). Another radiologist (radiologist B, with 10 years of experience) reviewed all ROIs manually segmented by radiologist A, showed the baseline clinical characteristics of patients in the our cohort, respectively.

ROIs were drawn along the edges of the pelvicalyceal effusion, aiming to encompass the effusion area while excluding kidney tissue, fat, calculi, blood vessels, or image artifacts to ensure data reliability. Radiomic features within and between annotators were extracted, calculating the Intraclass Correlation Coefficient (ICC), and features with an ICC $\geq$ 0.75 were included in subsequent research.

Radiomic feature extraction

In this study, radiomic features were extracted using the python3.7-based PyRadiomics version 3.0.1. Initially, features were extracted from the original images, covering aspects such as shape, size, intensity, and texture. To enhance the accuracy and efficacy of feature extraction, images were processed using a Gaussian-Laplacian filter (Laplacian of Gaussian, LOG), a common image enhancement technique that accentuates edges and details in an image. Wavelet transform, a multi-resolution analysis method, extracted features across different scales of the pelvicalyceal effusion. A total of 1834 radiomic feature parameters were extracted. See Table 1S for details.

Radiomic feature selection and model construction

Patient data for the training and validation sets were randomly stratified in a 7:3 ratio. To avoid overfitting, dimensionality reduction was applied to the extracted radiomic features, selecting meaningful features from the training set.

First, we performed a Mann–Whitney U test and feature screening for all radiomic features. Only the radiomic features with a p-value < 0.05 were kept. After this step is completed, 1156 features remain. Then, for features with high repeatability, Spearman's rank correlation coefficient was also used to calculate the correlation between features, and one of the features with correlation coefficient greater than 0.9 between any two features is retained. In order to retain the ability to depict features to the greatest extent, we use greedy recursive deletion strategy for feature filtering, that is, the feature with the greatest redundancy in the current set is deleted each time. After this, XX features were finally kept. After this step is completed, 299 features remain. At last, the least absolute shrinkage and selection operator (LASSO) regression model was used on the discovery data set for signature construction. Depending on the regulation weight λ, LASSO shrinks all regression coefficients towards zero and sets the coefficients of many irrelevant features exactly to zero. To find an optimal λ, tenfold cross-validation with minimum criteria was employed, where the final value of λ yielded minimum cross-validation error. The retained features with nonzero coefficients were used for regression model fitting and combined into a radiomics signature. Subsequently, we obtained a radiomics score for each patient by a linear combination of retained features weighed by their model coefficients. The Python scikit-learn package was used for LASSO regression modeling. After this step is completed, 14 features remain.

Selection and construction of clinical variable models

Univariate logistic regression analysis of clinical variables in the training set identified those with significant differences. These variables were then used in multivariate logistic regression analysis to construct a prediction model based on clinical variables. To ensure the accuracy and reliability of this model, its performance was thoroughly tested in both the training and validation sets.

Construction and evaluation of combined models

The building process of clinical signature is almost the same as rad signature. First the features used for building clinical signature were selected by baseline statistic whose p value < 0.05. We also used the same machine learning model in rad signature building process. Fivefold cross-validation and test cohort was set to be fixed for fair comparison.

After Lasso feature screening, we input the final features into the machine learning (nb) for risk model construction. Here, we adopt fivefold cross-verification to obtain the final Rad signature. Receiver operating characteristic (ROC) curves were plotted to assess the diagnostic performance of the predictive models, and the corresponding area under the curve (AUC), diagnostic accuracy, sensitivity, specificity, positive predictive value (PPV), and negative predictive value (NPV) were analyzed.

Furthermore, to intuitively and efficiently assess the incremental prognostic value of the radiomics signature to the clinical risk factors, a radiomics nomogram was presented on the validation data set. The nomogram combined the radiomics signature and the clinical risk factors based on the logistic regression analysis. To compare the agreement between the pyonephrosis prediction of the nomogram and the actual observation, the calibration curve was calculated.

Statistical analysis

SPSS (version 26.0, IBM) and R (version 4.2.1) software were employed for analysis. Continuous variables were first subjected to normality tests to determine data distribution characteristics. If data were homoscedastic and normally distributed, statistical description was through mean ± standard deviation, and group differences were compared using the t-test. If the data were not normally distributed, description was through interquartile range, and group differences were analyzed using the Mann–Whitney U test. Categorical variables were described using case numbers and percentages (%), with group differences assessed using the Chi-square test. Additionally, the DeLong test compared AUC values between groups, while the paired Chi-square test evaluated group differences in accuracy, sensitivity, specificity, and other metrics.

Abbreviations

AUC	Area under the curve
ANOVA	One-way analysis of variance
BMI	Body mass index
CI	Confidential interval
CT	Computed tomography
CRP	C-reactive protein
DCA	Decision curve analysis
ESWL	Extracorporeal shock wave lithotripsy
GFR	Glomerular filtration rate
HU	Hounsfield units
LMR	Lymphocyte–monocyte ratio
LR	Logistic regression
MRI	Magnetic resonance imaging
NB	Naive Bayes
NLR	Neutrophil–lymphocyte ratio
NPV	Negative predictive value
PCN	Percutaneous nephrostomy
PCNL	Percutaneous nephrostolithotomy
PCT	Procalcitonin
PLR	Platelet–lymphocyte ratio
PPV	Positive predictive value
RF	Random forest
ROC	Receiver operating characteristic
ROI	Region of interest
RUS	Retrograde ureteral stenting
SHACK	Severe hydronephrosis or atrophy of the contralateral kidney
SVM	Support vector machines
URSL	Ureteroscopic lithotripsy

Supplementary Information

The online version contains supplementary material available at https://doi.org/10.1186/s12938-024-01295-z.

Additional file 1.

Acknowledgements
Not applicable.

Author contributions
Yongchao Yan contributed to the analysis of the results and to the writing of the manuscript. Yunbo Liu contributed to the design and implementation of the research, Yize Guo and Bin Li were involved in collecting data. Yianjiang Li provided guidance and revisions for this article. Xinning Wang conceived the original and supervised the project.

Funding
Not applicable.

Availability of data and materials
The datasets used and/or analyzed during the current study are available from the corresponding author on reasonable request.

Declarations

Ethics approval and consent to participate
As this publication is a report that contains no identifiable content to the patient, this publication was exempt from ethical approval by the Human Research Protection Program (HRPP) and its Institutional Review Board (IRB) at the Ethics Committee of the affiliated hospital of Qingdao University. The requirement for written informed consent was waived by the Institutional Review Board (IRB) of The Affiliated Hospital of Qingdao University owing to the retrospective nature of the study.

Statistics and biometry
Xinning Wang kindly provided statistical advice for this manuscript. One of the authors has significant statistical expertise. No complex statistical methods were necessary for this paper.

Study subjects or cohorts overlap
Not applicable

Methodology
A single-center retrospective study conducted at one institution.

Animal studies
Not applicable.

Consent for publication
As this publication is a report that contains no identifiable content to the patient, this publication was exempt from ethical approval by the Human Research Protection Program (HRPP) and its Institutional Review Board (IRB) at the Ethics Committee of the affiliated hospital of Qingdao University. The requirement for written informed consent was waived by the Institutional Review Board (IRB) of The Affiliated Hospital of Qingdao University owing to the retrospective nature of the study.

Competing interests
The authors declare no competing interests.

Received: 15 July 2024 Accepted: 24 September 2024
Published online: 03 October 2024

References

1. Hesse A, Brändle E, Wilbert D, Köhrmann KU, Alken P. Study on the prevalence and incidence of urolithiasis in Germany comparing the years 1979 vs 2000. Eur Urol. 2003;44(6):709–13.
2. Tu MQ, Shi GW. He JY [Treatment of pyonephrosis with upper urinary tract calculi]. Zhonghua Yi Xue Za Zhi. 2011;91:1115–7.
3. Wang J, Zhou DQ, He M, et al. Effects of renal pelvic high-pressure perfusion on nephrons in a porcine pyonephrosis model. Exp Ther Med. 2013;5(5):1389–92.
4. Kumar LP, Khan I, Kishore A, Gopal M, Behera V. Pyonephrosis among patients with pyelonephritis admitted in department of nephrology and urology of a tertiary care centre: a descriptive cross-sectional study. JNMA J Nepal Med Assoc. 2023;61:258.
5. Ordonez M, Hwang EC, Borofsky M, Bakker CJ, Gandhi S, Dahm P. Ureteral stent versus no ureteral stent for ureteroscopy in the management of renal and ureteral calculi. Cochrane Database Syst Rev. 2019. https://doi.org/10.1002/14651858.CD012703.pub2.

6. Flukes S, Hayne D, Kuan M, et al. Retrograde ureteric stent insertion in the management of infected obstructed kidneys. BJU Int. 2015;115:31–4.
7. Tamburrini S, Lugara M, Iannuzzi M, et al. Pyonephrosis ultrasound and computed tomography features: a pictorial review. Diagnostics. 2021;11:2.
8. Li H, Xie F, Zhao C, et al. Primary mucinous adenocarcinoma of the renal pelvis misdiagnosed as calculous pyonephrosis: a case report and literature review. Transl Androl Urol. 2020;9(2):781–8.
9. Chang SH, Hsieh CH, Weng YM, et al. Performance assessment of the mortality in emergency department sepsis score, modified early warning score, rapid emergency medicine score, and rapid acute physiology score in predicting survival outcomes of adult renal abscess patients in the emergency department. Biomed Res Int. 2018. https://doi.org/10.1155/2018/6983568.
10. Wang Z, Yang G, Wang X, et al. A combined model based on CT radiomics and clinical variables to predict uric acid calculi which have a good accuracy. Urolithiasis. 2023;51(1):37.
11. Xu L, Yang C, Zhang F, et al. Deep learning using ct images to grade clear cell renal cell carcinoma: development and validation of a prediction model. Cancers. 2022. https://doi.org/10.3390/cancers14112574.
12. Liu H, Wang X, Tang K, et al. Machine learning-assisted decision-support models to better predict patients with calculous pyonephrosis. Transl Androl Urol. 2021;10(2):710–23.
13. Kuntz JA, Berent AC, Weisse CW, et al. Double pigtail ureteral stenting and renal pelvic lavage for renal-sparing treatment of obstructive pyonephrosis in dogs: 13 cases (2008–2012). J Am Vet Med Assoc. 2015;246(2):216–25.
14. Li AC, Regalado SP. Emergent percutaneous nephrostomy for the diagnosis and management of pyonephrosis. Semin Intervent Radiol. 2012;29(3):218–25.
15. Patodia M, Goel A, Singh V, et al. Are there any predictors of pyonephrosis in patients with renal calculus disease? Urolithiasis. 2017;45(4):415–20.
16. Chen DC, Potok OA, Rifkin D, et al. Advantages, limitations, and clinical considerations in using cystatin C to estimate GFR. Kidney360. 2022;3:10.
17. Odden MC, Tager IB, Gansevoort RT, et al. Age and cystatin C in healthy adults: a collaborative study. Nephrol Dial Transplant. 2010;25(2):463–9.
18. Ding L, Liu Z, Wang J. Role of cystatin C in urogenital malignancy. Front Endocrinol (Lausanne). 2022;13:1082871.
19. Boeri L, Fulgheri I, Palmisano F, et al. Hounsfield unit attenuation value can differentiate pyonephrosis from hydronephrosis and predict septic complications in patients with obstructive uropathy. Sci Rep. 2020;10(1):18546. https://doi.org/10.1038/s41598-020-75672-8.
20. Kaplan DM, Rosenfield AT, Smith RC. Advances in the imaging of renal infection Helical CT and modern coordinated imaging. Infect Dis Clin North Am. 1997;11(3):681–705.
21. Yuruk E, Tuken M, Sulejman S, et al. Computerized tomography attenuation values can be used to differentiate hydronephrosis from pyonephrosis. World J Urol. 2017;35(3):437–42.
22. Liu H, Wang X, Tang K, Peng E, Xia D, Chen Z. Machine learning-assisted decision-support models to better predict patients with calculous pyonephrosis. Transl Androl Urol. 2021;10(2):710–23. https://doi.org/10.21037/tau-20-1208.
23. Basmaci I, Sefik E. A novel use of attenuation value (Hounsfield unit) in non-contrast CT: diagnosis of pyonephrosis in obstructed systems. Int Urol Nephrol. 2020;52(1):9–14. https://doi.org/10.1007/s11255-019-02283-2.
24. Wang X, Tang K, Xia D, et al. A novel comprehensive predictive model for obstructive pyonephrosis patients with upper urinary tract stones. Int J Clin Exp Pathol. 2020;13(11):2758–66.
25. Ding C, Bao TY, Huang HL. Quantum-inspired support vector machine. IEEE Trans Neural Netw Learn Syst. 2022;33(12):7210–22.
26. Pellegrino E, Jacques C, Beaufils N, et al. Machine learning random forest for predicting oncosomatic variant NGS analysis. Sci Rep. 2021;11(1):21820.
27. Speiser JL, Miller ME, Tooze J, et al. A comparison of random forest variable selection methods for classification prediction modeling. Expert Syst Appl. 2019;134:93–101.
28. Rigatti SJ. Random forest. J Insur Med. 2017;47(1):31–9.
29. Zhang Z. Naive bayes classification in R. Ann Transl Med. 2016;4(12):241.
30. Kim YJ. Machine learning model based on radiomic features for differentiation between COVID-19 and pneumonia on Chest X-ray. Sensors. 2022;22:17.

Publisher's Note